The ISM local to the runaway star WR16

S. Cichowolski,[1]★† N. U. Duronea,[2]★† L. A. Suad,[1]† E. M. Reynoso,[1]†
A. Noriega-Crespo[3] and L. Bronfman[4]

[1]*Instituto de Astronomía y Física del Espacio (UBA, CONICET), CC 67, Suc. 28, 1428 Buenos Aires, Argentina*
[2]*Instituto Argentino de Radioastronomía (CCT-La Plata, CONICET; CICPBA), C.C. No. 5, 1894 Villa Elisa, Argentina*
[3]*Space Telescope Science Institute, 3700 San Martin Drive, Baltimore, DM 21218, USA*
[4]*Departamento de Astronomía, Universidad de Chile, Casilla 36, Santiago de Chile, Chile*

ABSTRACT

Massive stars leave their imprint on the interstellar medium as they radiate their energy and undergo episodes of mass ejection throughout their lives. In this paper, we analyse the case of the Wolf–Rayet star WR16 combining archival multiwavelength data with new molecular observations obtained with the Atacama Submillimeter Telescope Experiment (ASTE). Our results suggest that during the main-sequence phase, WR16 swept up the surrounding gas creating a molecular structure (which we call Component 1) which also contains very cold dust observed in the infrared band. In a subsequent stage of evolution, as an LBV, the star underwent mass eruptions that were later overrun by the fast winds of the current WR phase. The final result is the round nebula revealed by the optical and IR images, and the molecular clumps detected. We have also computed the peculiar velocity of WR16 using *Gaia* data and, accordingly, confirm it as a runaway star. We propose that several features observed in different wavelengths can be explained under a bow-shock scenario linked to the high velocity of WR16.

Key words: stars: massive – stars: Wolf–Rayet – ISM: structure.

1 INTRODUCTION

It is well known that, before core-collapse, very massive stars strongly modify the structure and dynamics of the interstellar medium (ISM) as a consequence of their stellar winds, strong ionizing photon fluxes, and, occasionally, proper motions (Weaver et al. 1977).

Throughout their lives, massive stars go through different evolutionary phases, in which they have different types of winds and generate around them a variety of structures. After leaving the main sequence, very massive stars enter the red supergiant (RSG) or luminous blue variable (LBV) phase, where they have dense, slow, dust-rich winds that expand into the ISM. These slow winds may expel more than half of the initial mass of the star, exposing its hot core and becoming a Wolf–Rayet (WR) star. Then, the strong and fast winds of the WR star sweep up and compress the previously ejected RSG or LBV material into a shell, while the newly developed UV flux ionizes the material, forming the so-called ring nebulae or

WR nebulae (Garcia-Segura & Mac Low 1995; Toalá & Arthur 2011).

Nebulae with various morphologies are often observed in the infrared around WR stars, as shown in Toalá et al. (2015) and references therein. On the contrary, although the molecular gas in LBV nebulae is also a subject of interest, there are only a few cases in which the presence of circumstellar molecular gas related to these nebulae have been determined by molecular studies, the most representative sources being AG Car (Nota et al. 2002) and G79.29+0.46 (Rizzo, Jiménez-Esteban & Ortiz 2008; Jiménez-Esteban, Rizzo & Palau 2010).

The Wolf–Rayet star WR16 presents a very conspicuous multiple ring nebula which, as described in Section 2, has been widely studied in the last few years. In particular, a very detailed work of this nebula was carried out by Duronea, Arnal & Bronfman (2013, hereafter Paper I). In that work, the authors reported three different molecular components and suggested that the one labelled as Component 3, which spatially coincides with the optical round nebula seen around WR16, could be related to the LBV phase of the star. As the authors pointed out, further high-spatial resolution observations of the inner part of the region would be needed to better analyse the properties of this component. With this aim, we have used the ASTE telescope to get new molecular data that allow us to study in more detail the local environment of the star.

★ E-mail: silcicho@gmail.com (SC); duronea@gmail.com (NUD)
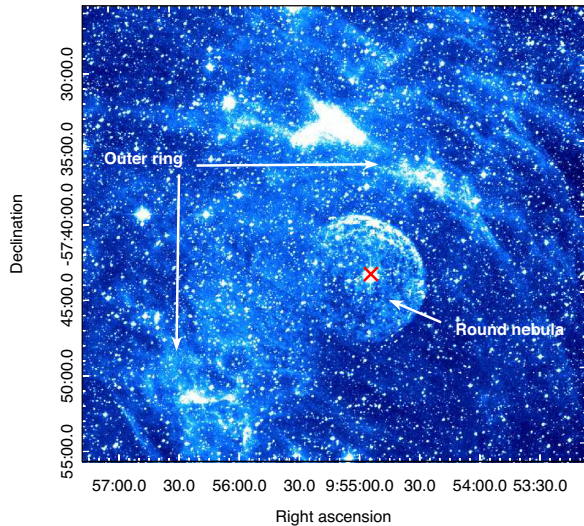† Member of the Carrera del Investigador Científico de CONICET, Argentina.

Figure 1. Super Cosmos H α image of the region around WR16. The red cross indicates the position of WR16.

Furthermore, new data have been release since the publication of Paper I, as those provided by the *Herschel* and *Gaia* satellites, that are useful to improve the description of the region. Thus, based on new molecular, infrared, optical, and radio continuum data, we present in this work a deeper analysis of the local environment around the WR star WR16.

2 WR16 AND ITS ENVIRONMENT

WR16 ($\equiv$HD86161), located in the inner Galaxy at $(l, b) = (281°079, -2°55)$, (α, δ)(J2000) = $(9^h 54^m 52^s.90, -57°43' 38''.275)$, is classified as a WN8h star (van der Hucht 2001).

The photometric distance to WR16 was estimated to be 2.37 kpc (van der Hucht 2001). Later on, based on the correlation between interstellar absorption lines and distance, Megier et al. (2009) used the interstellar Ca II line to estimate the distances to early-type stars, restricting the sample to objects beyond 1 kiloparsec. For WR16 they obtained a distance of 2231 $\pm$ 398 pc. Recently, based on the second *Gaia* data release (Gaia Collaboration 2018), Bailer-Jones et al. (2018) inferred distances from the parallaxes of 1.33 billion stars and obtained, for WR16, a distance of 2655^{+249}_{-210} pc. In the following we adopt this last value.

According to its proper motion as measured by *Gaia*, WR16 is a runaway star, with $(\mu_\alpha, \mu_\delta) = (-9.476 \pm 0.063, 4.975 \pm 0.052)$ mas yr^{-1} (Gaia Collaboration 2018). Moffat et al. (1998) had already suggested the same based on proper motions obtained from the *Hipparcos* astrometry satellite, from which they inferred a large tangential velocity of 123.9 $\pm$ 44.3 km s^{-1}, considering a distance of 4 kpc to WR16. In their work, Moffat et al. (1998) also pointed out that most of the runaway WR stars belong to the WN8 class, and that this goes along with the lack of them in clusters. One example is the star WR124 (WN8h) that has a very high peculiar motion and strongly affects its local ISM (van der Sluys & Lamers 2003; Cichowolski et al. 2008).

WR16 is one of the WR stars exhibiting a very conspicuous optical nebula, as can be seen in the image obtained from the Super COSMOS Sky Survey (Parker et al. 2005), shown in Fig. 1. This nebula was first detected by Marston et al. (1994), who included WR16 in the group of WR stars showing multiple rings. Further, the authors pointed out that there is evidence that WR16 has produced

up to three rings, a round nebula almost completely encircling the WR star and two outer, arc-like features towards the north-west, concentric with the main nebula, hereinafter the round nebula. Marston et al. (1994) suggested that the formation of multiple rings by WR stars may only occur via mass ejections from the star. The fact that the emission of the main nebula is sharper towards the north-west direction and diminished towards the south-east was associated with extinction due to the presence of molecular material in the way to the star (Toalá & Guerrero 2013) and, in a completely different scenario, to the large stellar proper motion, as suggested in Paper I.

Based on optical spectra and CO data, Marston et al. (1999) found that the inner part of the nebula is composed of highly N enriched material, suggested to be mass ejected in the red supergiant phase of the star. In this scenario, they concluded that the origin of the molecular gas observed near WR16 has also a stellar origin. In contrast, Marston et al. (1999) cannot rule out the possibility that the outer observed feature is swept-up interstellar gas.

Later on, Stock, Barlow & Wesson (2011) analysed spectroscopically the nebulae around several WR stars, including WR16, to quantify their degree of chemical enrichment. For WR16, Stock et al. (2011) pointed out that the nebula's composition is what one might expect from stellar outflows of a WN-type WR star.

The nebula around WR16 was also detected in the infrared. Marston & Morris (2009) inspected the *AKARI* images and found that the round optical shell is also seen at 90 μm, and that a more diffuse shell is detected at 140 μm. Based on the flux densities at 90 and 140 μm they inferred for the nebula a dust temperature around 25 K and a mass of 2.5 $M_\odot$. Later on, in Paper I, using HIRES data at 60 and 100 μm (Fowler & Aumann 1994), a dust temperature of about 28 K and a dust mass of 0.1 $M_\odot$ were estimated. Additionally, using *WISE* data, Toalá et al. (2015) carried out a morphological analysis of WR nebulae. They found for WR16 that the emission at 22 μm (*W4* band) is mostly coincident with the optical H α emission from ionized nebular material, and hence classified it as a WR bubble (*B* type in their nomenclature), which consist of nebulae that present a thin shell or bubble both in optical and IR, mostly in the *W4* band.

Another molecular analysis of the region was carried out in Paper I. Based on the analysis of both the ^{12}CO and ^{13}CO (1-0) emission in a region larger than the one observed by Marston et al. (1999), the authors of Paper I identified three molecular features (component 1, 2, and 3 in their nomenclature) probably related to different regions of the optical ring nebula. They suggest that components 1 and 2, at velocities[1] of -5 and -8.5 km s^{-1}, respectively, are associated with the external optical feature, while Component 3, at a velocity of -9.4 km s^{-1}, shows a good morphological agreement with the inner nebula reported by Marston et al. (1999). Finally, the mass contained in component 1 is suggested to be mostly composed of interstellar gas.

Toalá & Guerrero (2013) analysed *XMM–Newton* observations in the region of WR16 and find no evidence of diffuse emission related to the WR bubble, as was observed in similar WR bubbles. Toalá et al. (2017) pointed out that the presence or not of X-rays emission could be due to the spectral type of the star, in the sense that nebulae harbouring WN8h stars with relatively slow stellar winds are not detected in the *X* band, while those having central WN4-6 stars with faster winds, have been observed in X-rays (e.g. S308,

---

[1]All the velocities in this work are referred to the local standard of rest (LSR).

NGC 2359, and NGC 6888). Nevertheless, since the sample of WR nebulae analysed is small, they concluded that the properties of the X-ray-emitting gas may also depend on other stellar and/or nebular parameters.

The stratified morphology of the close environs around WR16 at optical, infrared, and millimeter emission, as well as its complex kinematics and composition makes this star a key piece to better understand episodic events associated with the evolution of a star previous to the WR phase. This encouraged us to perform a more thorough and detailed study of the interstellar medium around this star using new and archival data.

3 OBSERVATIONS AND DATA BASES

3.1 Molecular observations

The molecular observations were obtained in 2015 November with the 10-m Atacama Submillimeter Telescope Experiment (ASTE; Ezawa et al. 2004, 2008). We have used the DASH345 instrument, a two-sideband single-polarization heterodyne receiver, tunable in a LO frequency band from 327 to 370 GHz at observable frequency range from 321 to 376 GHz. The XF digital spectrometer was tuned to a bandwidth and spectral resolution of 128 MHz and 125 kHz, respectively. The spectral resolution was 0.11 km s^{-1}, the half power beamwidth (HPBW) is $\sim$22 arcsec and the main beam efficiency (η_{mb}) is 0.65. Observations were obtained in the on-the-fly (OTF) mode, centred on RA, Dec. (J2000) = ($9^h54^m52\overset{s}{.}9$, $-57°43'35\overset{''}{.}7$), with two orthogonal scan directions along RA and Dec. (J2000). We observed the lines CO(3-2) (345.796 GHz) and HCO$^+$(4-3) (356.734) simultaneously in a region of $\sim$12 arcmin $\times$ 12 arcmin in size. The spectra were reduced with NOSTAR[2] using the standard procedure.

For the molecular analysis, we also used SEST CO(2-1) data that were kindly provided to us by A. P. Marston in 2008 (see Marston et al. 1999), and NANTEN CO(1-0) obtained in 2001 (see Paper I).

3.2 H I and radio continuum data

Current radio surveys are of little use to inspect the surroundings of WR16 with enough resolution and sensitivity. In Paper I, the radio continuum data at 4.8 GHz were obtained from the Parkes-MIT-NRAO (PMN) survey. At the location of WR16, the survey contains observations performed with the Parkes 64-m antenna. However, the beam size ($\sim$5 arcmin $\times$ 5 arcmin) is comparable to the diameter of the ring nebula ($\lesssim$8 arcmin), which hampers a detailed study. To render an acceptable resolution, observations must be performed using interferometeric techniques, and only two radio interferometers, the Australia Telescope Compact Array (ATCA) and the Molonglo Observatory Synthesis Telescope (MOST), offer public surveys covering an area compatible with the Galactic longitude of WR16. The Southern Galactic Plane Survey (SGPS; McClure-Griffiths et al. 2005), which includes both H I and continuum emission data from the ATCA, is limited to $-1° \leq b \leq +1°$, and WR16 lies more than 1° away south of this band. On the other hand, the radio continuum emission towards WR16 at 843 MHz from the Molonglo Galactic Plane Survey (MGPS-2; Murphy et al. 2007) is affected by strong sidelobes introduced by the bright nearby H II region RCW 46.

[2]http://alma.mtk.nao.ac.jp/aste/guide/otf/reduct-e.html

Table 1. Parameters of ATCA observations.

	Continuum	H I line
Project code	C961	
Date/configuration	14; 17Oct2001/EW352	
	1–2Jan2002/EW352	
	16–20Mar2002/EW367	
Central frequency (MHz)	1384	1420
Bandwidth (MHz)	128	4
N° channels	32	1024
Maximum angular scale	$37\overset{'}{.}3$	$36\overset{'}{.}3$
Synthesized beam	$98\overset{''}{.}0 \times 87\overset{''}{.}7$	$149\overset{''}{.}5 \times 132\overset{''}{.}5$
Position angle (P.A.)	$-61\overset{\circ}{.}1$	$47\overset{\circ}{.}6$
Convolved beam	100 arcsec $\times$ 100 arcsec	130 arcsec $\times$ 130 arcsec
Theoretical sensitivity	1.5 mJy beam^{-1}	3 K
Measured sensitivity	2 mJy beam^{-1}	5 K

To obtain the best possible set of maps, we then processed from scratch archival radio observations performed during 2001 and 2002 towards this region with the Australia Telescope Compact Array (ATCA) in the configurations EW 352 and EW 367 under project C961. The region was observed simultaneously in the H I 21-cm line and in radio continuum. The continuum data consist of 32 channels spanning through a bandwidth of 128 MHz centred at 1384 MHz, while the H I line was recorded over 1024 channels covering a 4 MHz bandwidth (equivalent to 0.82 km s^{-1}). Pointings were arranged in an hexagonal mosaic with a 23 arcmin grid separation and were observed as snapshots during 60 s over a wide range of hour angles. All observation parameters are summarized in Table 1.

Standard data reduction was performed with the MIRIAD software package (Sault, Teuben & Wright 1995), using PKS B1934−638 for flux and bandpass calibration and PKS B0843−54 for phase calibration. For the H I data, the continuum component was subtracted by fitting a linear baseline through a set of line-free channels in the Fourier domain. All pointings in the mosaic were cleaned together with a joint approach using the MIRIAD task MOSMEM. For the H I data, the solutions converged for all channels. Finally, the clean components were convolved with a 130 arcsec $\times$ 130 arcsec and a 100 arcsec $\times$ 100 arcsec beam for the line and continuum images, respectively. Thus, the resolution of the continuum image is improved by almost an order of magnitude as compared to the image in Paper I. The spectral resolution of the H I cube is 0.82 km s^{-1}. To sample extended structures, filtered out by interferometric observations, short spatial frequencies were added to the H I cube. For this purpose, single dish data from the Parkes Galactic All Sky Survey (GASS; McClure-Griffiths et al. 2009; Kalberla et al. 2010; Kalberla & Haud 2015) were combined with the ATCA H I data in the Fourier domain using the IMMERGE routine in MIRIAD. No tapering was applied to the low-resolution cube.

3.3 Infrared data

To study different components in the nebula around WR16, we have retrieved data available in the archives from mid-infrared (mid-IR) to far-infrared (FIR) from the *Wide-field Infrared Survey Explorer (WISE)* and the *Herschel Space Observatory*. The *Herschel* images were observed under project ID OT2-amarston-2. The 22 μm (*W*4) emission from *WISE* has a full width at half-maximum (FWHM) of 12 arcsec. The *Herschel* images used the photometric array camera and spectrometer (PACS) and the spectral and photometric imaging receiver (SPIRE). The PACS survey includes the emission
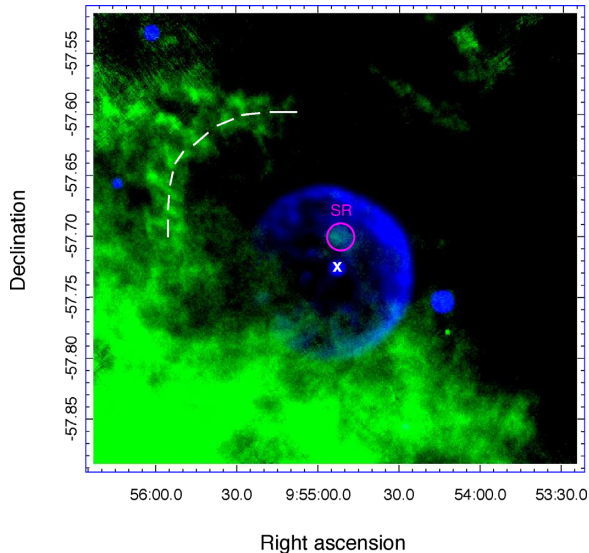
Figure 2. Infrared image of the region of WR16. Green: *Herschel* emission at 160 μm. Blue: *WISE* emission at 22 μm. The white cross shows the position of WR16. The white dashed line indicates the position of the arc-like feature mentioned in the text.

at 70, 100, and 160 μm, with FWHM of 5.5, 6.7, and 11 arcsec, respectively. The SPIRE survey provides the 250, 350, and 500 μm data, whith FWHM of 18, 25, and 37 arcsec, respectively.

4 RESULTS

4.1 Infrared emission

Making use of the data presented in Section 3.3, we analysed the dust properties and distribution around WR16, specially looking for counterparts of the features observed at optical wavelengths (see Fig. 1).

Fig. 2 shows the emission detected at 22 and 160 μm. In this image, the round nebula, known to be composed by ejected gas (Marston et al. 1999), is clearly observed at 22 μm (in blue), while at 160 μm (in green) it is barely detected, except for a small region (SR) as indicated in Fig. 2. This nebula is also detected at 70 and 100 μm, as can be seen in Fig. 3, where the *Herschel* images at 70, 100, 160, 250, 350 and 500 μm are shown. As observed at 22 μm, the emission of the round nebula is not uniform. Instead, the western hemisphere is brighter than the eastern one. Further, in the north-western region, where the outer ring is seen at optical wavelengths, two small IR features, located at $(\alpha, \delta) = (9^{\rm h}\,54^{\rm m}\,20^{\rm s}$, $-57^\circ6)$ and $(\alpha, \delta) = (9^{\rm h}\,54^{\rm m}$, $-57^\circ54)$, are detected at 160 μm (see Fig. 2). However, they do not seem to be the IR counterpart of the optical outer ring, since their spatial locations are not coincident.

Another noticeable structure in Fig. 2 is the arc-like feature seen at 160 μm, which is indicated by a dashed line. As seen in Fig. 3, this feature is also observed at 250, 350, and 500 μm.

In order to characterize the dust originating the detected emission, we obtained the flux densities of the round nebula at 22, 70, and 100 μm, and of the arc-like feature at 160, 250, 350, and 500 μm. The values obtained are presented in Table 2. To obtain the flux densities related to the round nebula, we first convolved the PACS data at 70 and 100 μm down to the spatial resolution of the *WISE* data at 22 μm (12 arcsec). Similarly, for the arc-like feature, we convolved the data at 160, 250, and 350 μm down to the resolution of the

500 μm data (37 arcsec). We considered a circular region centred at $(\alpha, \delta) = (9^{\rm h}54^{\rm m}53^{\rm s}, -57^\circ43'38'')$ with a 4 arcmin radius for the round nebula and for the arc structure, a region limited within the emission levels of 0.016 Jy pix^{-1}, 157, 91, and 38.7 MJy sr^{-1} at 160, 250, 350, and 500 μm, respectively.

One of the main difficulties in estimating flux densities is background subtraction. To achieve this, we estimated the flux densities of selected areas next to the region under study, avoiding other high-contrast features. As can be seen in Fig. 3, the background is quite inhomogeneous, specially towards the south. The average of the values obtained in different regions was assumed as the background emission. Keeping in mind the assumptions made in determining both the area covered by the region under study (particularly critical for the arc structure) and the background emission, we estimate an uncertainty in the flux measurements of at least 30 percent.

Having the infrared flux densities (see Table 2), we can estimate the dust temperature ($T_{\rm d}$) of the observed features by fitting a Planck function. Fig. 4 (upper panel) shows the Planck distribution for $T_{\rm d} = 65$ K together with the three flux densities estimated for the round nebula, while Fig. 4 (bottom panel) displays the Plank function for $T_{\rm d} = 11$ K with the flux densities estimated for the arc feature overlaid. These plots indicate that the dust contained in the round nebula is quite warm, in contrast with the low temperature of the dust associated with the arc feature. The dust temperature obtained in this work for the round nebula (65 K) is considerably higher than the values found by Marston & Morris (2009) (28 K) and in Paper I (25 K). This difference could be attributed to the fact that we are using data with higher resolution than Marston & Morris (2009) and Duronea et al. (2013), who made use of data from *IRAS* and *AKARI* (which are likely dominated by confusion in the larger beam). Moreover, since we added to the analysis *WISE* data at 22 μm, where the round nebula is striking, we are getting the temperature of the smaller dust particles. We believe that the temperature of about 25 K estimated in previous works is related to colder dust present in the interstellar medium.

Knowing the $T_{\rm d}$, the dust mass ($M_{\rm d}$) can be estimated using the expression derived by Hildebrand (1983)

$$M_{\rm d} = \frac{F_{70}\, d^2}{B_{70}(T_{\rm d})\, k_{70}}. \tag{1}$$

where d is the distance to the WR nebula, $B_{70}(T_{\rm d})$ is the blackbody intensity at $T_{\rm d}$ for $\lambda = 70$ μm, and $k_{70} = 230$ cm^2 gr^{-1} (Hutsemekers 1997) is the mass absorption coefficient.

For the round nebula we obtained $M_{\rm d} = 6.7 \times 10^{-4}$ M$_\odot$ for $T_{\rm d} = 65$ K. This value is consistent for dust in LBV-type nebulae, as shown by Hutsemekers (1997). In his study, based on *IRAS* 25 and 60 μm data, Hutsemekers (1997) found dust temperatures ranging from 55 to 133 K and dust masses between 3.1×10^{-4} and 3.8×10^{-2} (see his Table 2), and showed that there is a correlation between the dust temperatures and the radius of optical nebulae, with the hotter dust in the smaller bubbles, as expected if the dust is mixed with the ionized gas close to the star. In this sense, assuming a radius of 3.5 pc (or $0^\circ.075$ at 2665 pc) for WR16, our estimations of $T_{\rm d}$, using similar wavelengths (22 and 70 μm) as Hutsemekers (1997), are in perfect agreement with this relation (see his Fig. 1). As an example, Hutsemekers (1997) pointed out that the LBV nebula around WR136 has a radius of 3.7 pc and a dust temperature of 62 K. Based on *Spitzer* 24 μm and *Herschel* 70 μm data, Agliozzo et al. (2014) calculated the dust temperature of warm dust grains distributed in three concentric rings around the nebula LBV G79.29+0.46 and obtained values between 60 and 85 K. In a recent work, Agliozzo et al. (2019) using *Spitzer*, *Herschel*, and
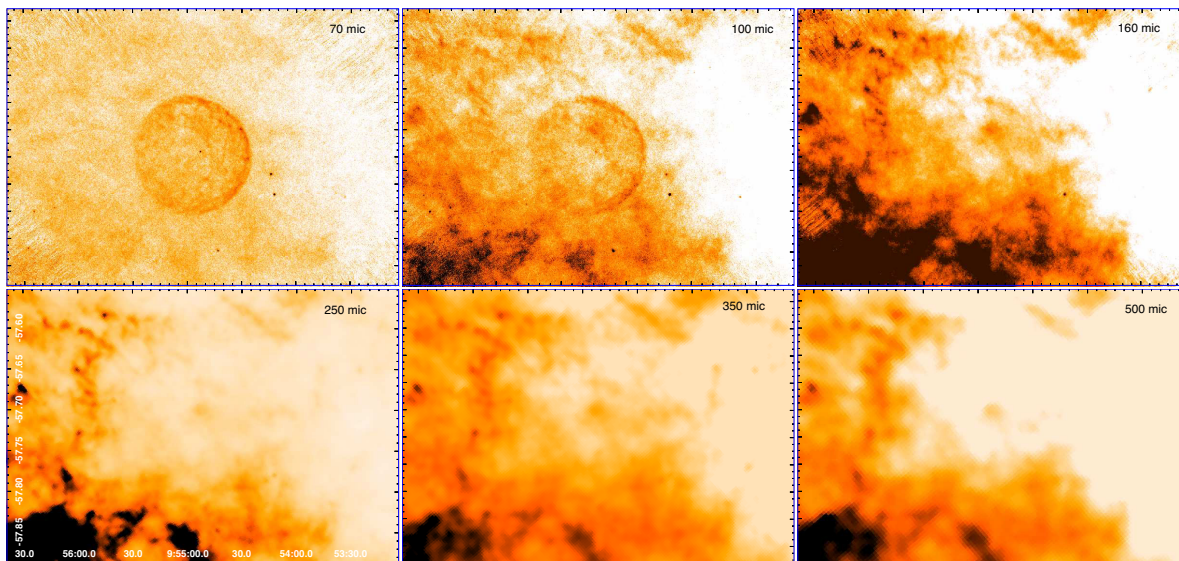
Figure 3. *Herschel*, PACS, and SPIRE, images of the region of WR16. The wavelength corresponding to each image is indicated in the upper right corner of each panel. Regions with more infrared emission are shown as dark regions.

Table 2. Flux densities of the round nebula and the arc feature.

λ (μm)	Flux (Jy) Round nebula	Flux (Jy) Arc feature
22	7.3	–
70	23.5	–
100	18.1	–
160	–	43.5
250	–	46.0
350	–	45.1
500	–	17.2

Note. Flux density uncertainties are estimated to be at least 30 per cent.

ALMA data obtained an average $T_d \sim 70$ K in the nebula around LVB RMC 143 which is located in the outskirts of the 30 Doradus complex.

4.2 H I and radio continuum

Fig. 5 shows the radio continuum emission at 1.4 GHz in a region around WR16, marked by a pink cross near the centre. Two bright sources in the area, pointed by numbers 1 and 2 and catalogued as PMN J0958−5757 and PMN J0951−5750, respectively, can potentially affect the image quality, and we do not discard that some of the features are actually artefacts introduced by sidelobes or grating rings from these two sources. The noise level is $\sigma \sim 2$ mJy beam^{-1}. Black contours are plotted at 12 and 18 mJy beam^{-1}, i.e. at about 6σ and 9σ. We do not detect the inner nebula (Feature 1) reported in Paper I probably because the snapshot observing mode detects strong emission only (at the present resolution, this feature is weaker than 2σ) and the structure scale is large enough to be filtered out by the interferometer.

A close up of the area enclosed in Fig. 5 is displayed in Fig. 6, where radio continuum contours are overlaid on the optical image. We notice that a radio feature appears at the position where the Hα emission is brightest, towards its north-western part. This radio
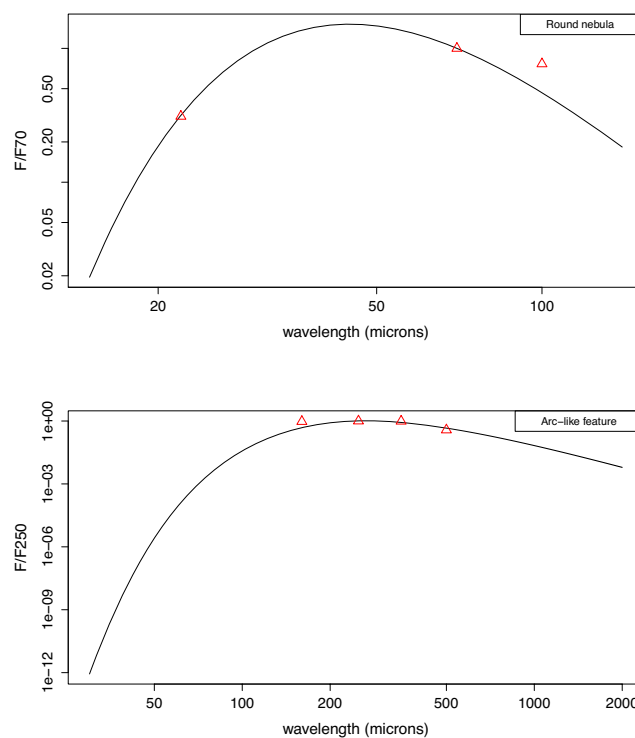

Figure 4. *Upper panel:* A comparison of the mid-far-IR observations of the round nebula normalized to the 70 μm flux density (open triangles), with a Planck function at 65 K. *Bottom panel:* Far IR flux densities (open triangles) normalized to the 250 μm of the arc-like feature compared with a Planck function at 11 K.

feature is parallel to the arc and has a flux density of $\sim$50 mJy. Nearly 4 arcmin north from this radio feature, there is another feature of comparable size and elongation, although weaker (flux density of $\sim$30 against 50 mJy), which surprisingly lies over the brightest part of an outer Hα arc concentric with the WR16 ring nebula.

Concerning H I, we have inspected the whole data cube in search for any structure that could be related to WR16. We regard a
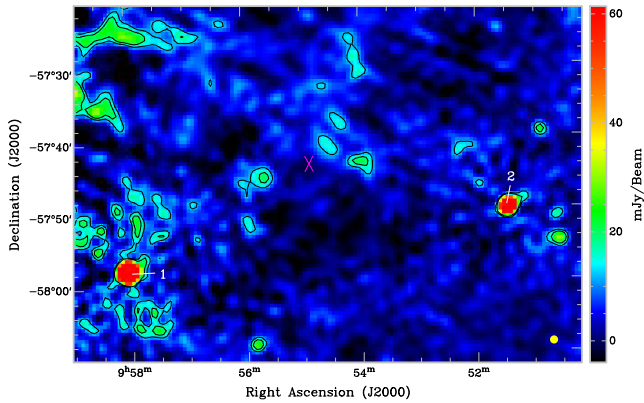
Figure 5. ATCA image of the radio continuum emission at 1.4 GHz. WR16 is plotted with a pink cross near the centre. The two bright sources indicated with numbers 1 and 2 are PMN J0958−5757 and PMN J0951−5750, respectively. Black contours at 12 and 18 mJy beam^{-1} are overlaid. The rms noise level is ~2 mJy beam^{-1}. The beam, 100 arcsec × 100 arcsec, is represented with a yellow filled circle at the bottom right corner.
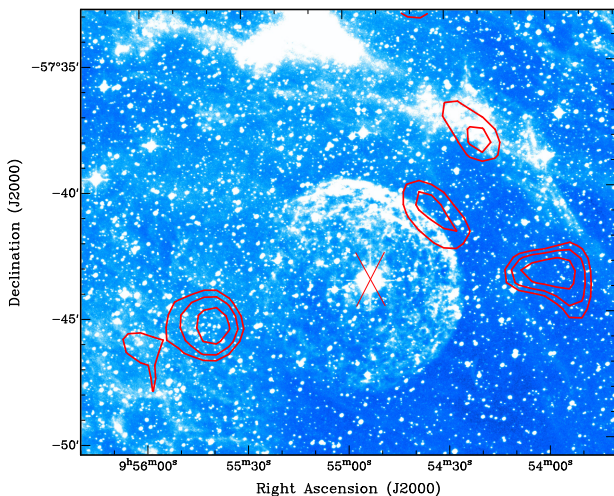

Figure 6. Hα image of the ring nebula around WR16. The red cross indicates the position of WR16. ATCA radio continuum emission at 1.4 GHz is overlaid with contours at 12, 14.5, and 18 mJy beam^{-1}.

structure as candidate if it displays any morphological distribution suggestive of a physical association with WR16 and it is observed in at least five consecutive channels (see Arnal 1992). We also tried to find any feature that could be interpreted as a bow-shock structure, as the one found by Cichowolski et al. (2008) around WR124. We did not find any clear signature of the action of WR16 on the H I gas.

4.3 Molecular emission

4.3.1 Molecular components

To analyse the close molecular environments around WR16, we used ASTE data obtained in a region ~12 arcmin × 12 arcmin around the star (see Section 3.1). This analysis will also allow us to study in more detail the molecular gas associated with the inner nebula seen at IR and optical wavelengths.

For the sake of completeness we inspect the CO emission in the entire velocity interval, although for our analysis, we will mostly

focus on the molecular gas component around ~−9.4 km s^{-1}, which was identified as Component 3 in Paper I. This component seems to be physically associated with the inner round nebula around WR16 and was associated by the authors with a possible later stage on the episodic evolution of the nebular environment. It is worth mentioning that no emission of HCO$^+$(4−3) was detected in any velocity range in our data set, which suggests that the molecular gas associated with the close environments of the nebula is not very dense ($\lesssim$10^6 cm^{-3}).

In Fig. 7, we show the CO(3−2) emission overlaid on to the *Herschel* 70 μm continuum emission. To make a more reliable morphological analysis and comparison between both emissions, the 70 μm emission has been convolved down to a common spatial resolution of 22 arcsec. In this figure we show three different molecular structures that have been detected in the velocity intervals from −7.2 to −3.9, −9.4 to −8.1, and −10.6 to −9.4 km s^{-1}. The molecular component in the velocity range from −7.2 to −3.9 km s^{-1} (Fig. 7, upper panel) consists of three clumpy features located approximately at RA, Dec.(J2000) = (9^{h}54^{m}57^s, −57°38′00″) (labelled in Fig. 7 as clump *a*), RA, Dec. (J2000) = (9^{h}55^{m}19^s, −57°38′39″) (labelled as clump *b*), and RA, Dec. (J2000) = (9^{h}55^{m}22^s, −57°47′20″) (labelled as clump *c*). As can be seen from the figure, these clumps seem to be part of a larger structure (extending beyond the area covered with ASTE) which very likely corresponds to the molecular emission identified as component 1 in Paper I (see Fig. 2 there). This structure deserved considerable attention and its physical properties were thoroughly determined in the previously mentioned work, but some of them will be re-estimated for clumps *a*, *b*, and *c* for comparison purposes in Section 4.3.2.

As mentioned before, we will mostly concentrate our analysis in the molecular gas around −9.4 km s^{-1}; therefore, the molecular structures detected at velocity ranges from −9.4 to −8.1 and −10.6 to −9.4 km s^{-1} (Fig. 7, middle and lower panels, respectively) will be also analysed. In the velocity interval from −9.4 to −8.1 km s^{-1} a small molecular clump can be noticed at RA, Dec. (J2000) = (9^{h}54^{m}52^s, −57°41′53″) (labelled in Fig. 7 as clump *d*) projected on to the nebula and coincident with a small IR structure (indicated as SR in Fig. 2) near its inner edge. In this velocity interval, another small U-shaped structure is seen approximately at RA, Dec. (J2000) = (9^{h}55^{m}21^s, −57°39′18″), which is a residual emission from clump *b* and will be not taken in consideration for the rest of the analysis. In the velocity interval from −10.6 to −9.4 km s^{-1}, three molecular clumps are noticed centered approximately at RA, Dec. (J2000) = (9^{h}54^{m}28^s, −57°43′01″) (labelled as clump *e*), RA, Dec. (J2000) = (9^{h}54^{m}27^s, −57°46′18″) (labelled as clump *f*), and RA, Dec. (J2000) = (9^{h}54^{m}20^s, −57°48′22″) (labelled as clump *g*). For the sake of clarity in Fig. 7 we have encompassed clumps *f* and *g* with green dotted lines. Clump *e* appears projected on to the brightest part of the IR nebula, while clump *f* seems to perfectly delineate its southwestern border closely following the ring-shaped geometry. The characteristics and spatial location of clumps *d*,*e*, *f*, and *g* may explain the morphology of Component 3 reported in Paper I at ~−9.45 km s^{-1}, observed with undersampled low-spatial resolution NANTEN observations. The morphological coincidence of the clumps with the IR nebula, particularly clump *f*, supports their mutual physical association. Although clump *g* is not projected on to the IR nebula, it seems to be physically associated with clump *f* since a connecting CO emission of about 0.7 K (~17σ) is observed between both clumps. The association between clumps *f* and *g* is also kinematical, since both clumps are detected almost in the same velocity interval.
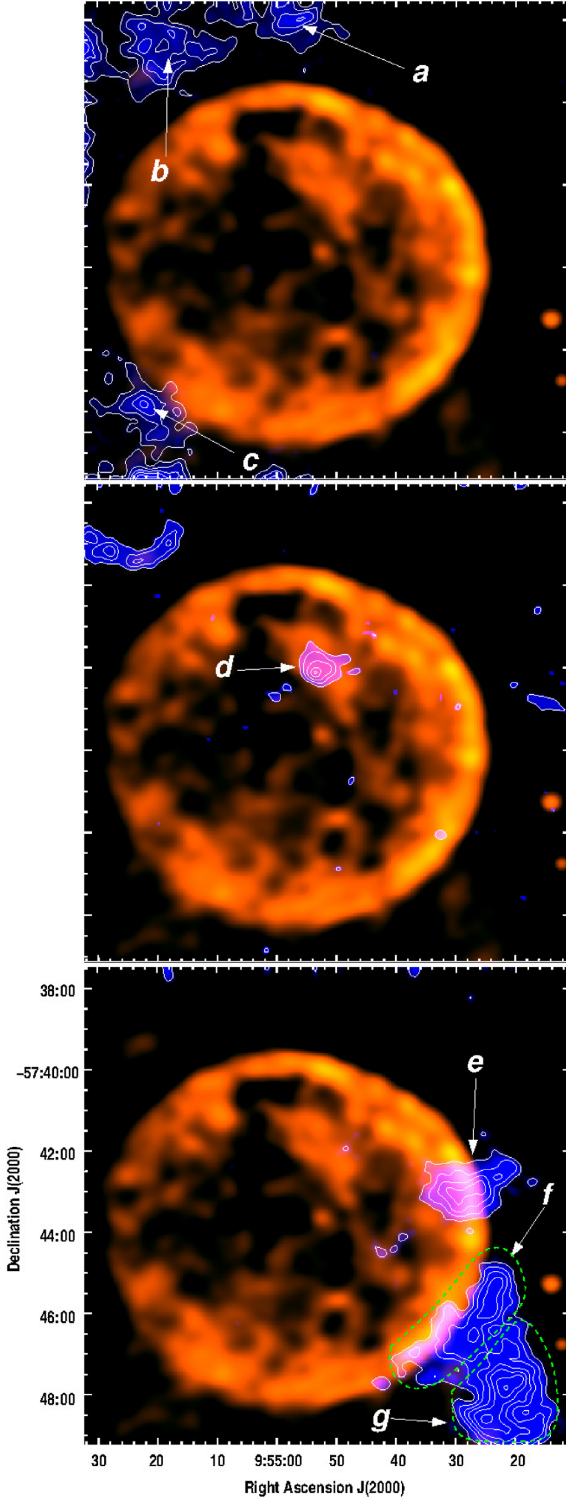
Figure 7. Composite image of the CO(3−2) emission (blue colours and white contours) and the *Herschel* 70 μm emission smoothed to a spatial resolution of 22 arcsec (red colour). *Top panel:* CO emission in the velocity interval from −7.2 to −3.9 km s^{-1}. Contour levels are 0.2 (∼8 rms), 0.3, 0.4, and 0.5 K km s^{-1}. *Middle panel:* CO emission in the velocity interval from −9.4 to −8.1 km s^{-1}. Contour levels are 0.2 (∼4.5 rms), 0.35, 0.5, 0.65, and 0.7 K km s^{-1}. *Bottom panel:* CO emission in the velocity interval from −10.6 to −9.4 km s^{-1}. Contour levels go from 0, 3 K km s^{-1} (∼6.5 rms) to 1.3 K km s^{-1} in steps of 0.2 K km s^{-1}.

4.3.2 *Physical properties of clumps a–f*

In Table 3, we show some observational parameters and physical properties estimated for the molecular clumps identified in the previous section. To estimate the mass of the clumps we use the relation between the H$_2$ integrated column density and the CO integrated emission

$$N_X(\text{H}_2) = X \times \frac{\int T_{\text{mb}}(\text{CO})}{0.7} \, \text{dv}, \tag{2}$$

where X is an empirical factor that has been shown to be roughly constant for the ^{12}CO(1−0) line in Galactic molecular clouds and lies in the range $(1–3) \times 10^{20}$ cm^{-2} (K km s^{-1})$^{-1}$, as estimated by the virial theorem and γ-ray emission (Bloemen et al. 1986; Solomon et al. 1987; Bertsch et al. 1993; Digel et al. 1996; Strong & Mattox 1996). In this paper, we adopt $X = 1.6 \times 10^{20}$ cm^{-2} (K km s^{-1})$^{-1}$ (Hunter et al. 1997). Since we use the integrated intensity emission of the CO(3−2) line, we need to adjust the value of $N_X(\text{H}_2)$ in equation 2 using a correcting factor of ∼0.7 (Oka et al. 2012). The total hydrogen mass, $M_X(\text{H}_2)$, is then calculated using

$$M_X(\text{H}_2) = \mu \, m_{\text{H}} \sum A_{\text{clump}} \, N_X(\text{H}_2) \, d^2, \tag{3}$$

where μ is the mean molecular weight, assumed to be 2.8 (considering a relative helium abundance of 25 per cent per mass), m_{H} is the hydrogen atom mass, A_{clump} is the area subtended by the CO clump (estimated using the first contour level indicated in Fig. 7), and d is the kinematical distance. The volume density, $n_X(\text{H}_2)$, was derived assuming spherical geometry for each clump and adopting an effective radius $R_{\text{eff}} = \sqrt{A_{\text{clump}}/\pi}$.

In the last three columns of Table 3, we also show the values derived from Gaussian fitting of the averaged spectra obtained in the direction of each clump, which will be used for the large velocity gradient (LVG) analysis (see below).

As expected, values of $M_X(\text{H}_2)$ derived for clumps *a*, *b*, and *c* are significantly lower than those obtained in Paper I for molecular clouds of Component 1 (see Table 1 there), since our ASTE observations only cover a reduced section of the surroundings of the nebula and the clumps are only a small fraction of the whole molecular component. On the other hand, the column densities $N_X(\text{H}_2)$ obtained for the clumps are about five times lower than those derived for Component 1 using factor X (see Table 1 in Paper I), although we speculate that this discrepancy could be due to the fact that clumps *a*, *b*, and *c* are closer to the nebula and are not tracing the densest regions of Component 1 (see Fig. 2 in Paper I). Moreover, the correction factor used of 0.7 between the integrated intensity of the CO(1−0) and CO(3−2) lines, represents a further source of uncertainty. For the case of volume densities, values lower than 105 cm^{-3} were derived for the clumps. Low volume densities were also expected since, as mentioned before, no emission of the high density tracer HCO$^+$(4−3) ($n_{\text{crit}} \sim 10^6$ cm^{-3}) was detected. However, the detection of the CO(3−2) line ($n_{\text{crit}} \sim 10^4$ cm^{-3}) suggests that volume densities could be somewhat higher than those indicated in Table 3. Furthermore, a higher density molecular gas, capable of surviving in the close harsh environment around a massive star, makes a more reliable scenario. This casts some doubts about using the factor X to derive $n_X(\text{H}_2)$ in a rarefied and highly processed molecular environment around a WR star (see Paper I for a brief discussion). For the case of WR 16, the observational evidence suggests that the detected CO could be either interstellar gas accumulated and disturbed by the stellar wind, the remains of the parental molecular cloud affected by the destructive action of the powerful stellar UV field, or even the results of several episodic

Table 3. Observed parameters and physical properties estimated for the CO clumps.

Clump	A_{clump} (10^{-7} sr)	R_{eff} (pc)	$\int T_{mb}$ (CO) (K km s^{-1})	N_X (H$_2$) (10^{20} cm^{-2})	M_X(H$_2$) (M$_\odot$)	n_X (H$_2$) (cm^{-3})	Line	T_{peak} (K)	v_{peak} (km s^{-1})	FWHM (km s^{-1})
a	1.19	0.51	0.96	2.2	3.9	105	(2−1)	1.61	−6.06	2.1
							(3−2)	0.53	−5.93	1.5
b	2.76	0.77	0.95	2.1	8.8	70	(2−1)	1.88	−4.66	1.8
							(3−2)	0.41	−4.53	1.4
c	1.71	0.61	0.89	2.0	5.5	85	(2−1)	1.82	−4.92	1.3
							(3−2)	0.43	−4.97	1.4
d	0.65	0.37	0.50	1.2	1.3	85	(2−1)	0.71	−8.71	1.9
							(3−2)	0.21	−8.66	1.4
e	1.79	0.62	0.69	1.6	4.5	50	(2−1)	1.83	−9.85	0.9
							(3−2)	0.56	−9.96	0.9
f	2.71	0.77	0.70	1.6	6.3	35	(2−1)	2.11	−10.02	1.0
							(3−2)	0.58	−9.91	0.9
g	3.28	0.84	0.91	2.1	10.4	50	(2−1)	3.05	−10.06	1.1
							(3−2)	0.02	−10.00	1.0

stellar molecular ejections (Marston et al. 1999; Stock et al. 2011; Duronea et al. 2013). Then, the detected molecular gas around WR 16 could have physical conditions which are different from those of the general interstellar medium.

We have also performed an analysis using the non-LTE LVG formalism (Scoville & Solomon 1973; Goldreich & Kwan 1974) for radiative transfer of molecular emission lines. We used the LVG code implemented as part of the MIRIAD[3] package of the Submillimeter Array (SMA). For a given kinetic temperature (T_k), this program estimates the line radiation temperature of a molecular transition as a function of the molecular column density (normalized by the line width FWHM) and the H$_2$ volume density. We have used the ASTE CO(3−2) line data, and the CO(2−1) line data obtained with SEST (see Section 3.1). In order to work with a directly comparable T_{mb} scale, the CO(3−2) line data have been convolved down to a common spatial resolution of 45 arcsec. The difficulty involved in this method is the need of making assumptions either about the column density or the kinetic temperature, which are not always easy to corroborate. Then, we have modelled the CO emission assuming suitable temperatures according to their characteristics and thermal coupling between the dust and molecular gas. For the cases of clumps *a*, *b*, and *c*, as mentioned before, they seem to be part of a larger structure, which very likely corresponds to the molecular emission identified as Component 1 in Paper I, and for which a dust temperature of ∼11 K was derived (see Section 4.1). On the other hand, for clumps *d*, *e*, *f*, and *g*, which are believed to be associated with the inner round nebula around WR16, a temperature of 65 K has been adopted (see Section 4.1). For each kinetic temperature, we modelled the CO(3−2) intensity line and the CO(3−2) to (2−1) line ratio on 50 × 50 model grids over a volume density range n(H$_2$) = 10–10^6 cm^{-3} and a normalized CO column density range N(CO)/Δv = 10^{13}–10^{18} cm^{-2} (km s^{-1})$^{-1}$. For the analysis, we compared the models with observational values derived from Gaussian fitting of the spectra obtained on the temperature peaks over an area corresponding to the clump (see Table 3). Volume H$_2$ densities and normalized CO column densities are obtained from the plots of the models (not shown here). The masses of the clumps tabulated in the last column of Table 4 were estimated using obtained values of N(CO) and equation (3). It is worth pointing out that since we have only two transitions, the LVG fitting allows us to determine

Table 4. Physical properties estimated for the CO clumps from LVG analysis.

Clump	T_K (K)	N (CO) (10^{16} cm^{-2})	n_{H_2} (cm^{-3})	M (H$_2$) (M$_\odot$)
a	11	≳1.4	≲13 000	>2
b	11	≳1.3	≲3000	>5
c	11	≳0.5	≲12 000	>1
d	65	≳1.9	≲130	>2
e	65	≳0.22	≲250	>0.7
f	65	≳0.64	≲210	>2.8
g	65	≳0.93	≲270	>4.8

upper limits for the H$_2$ volume density and lower limits for the CO column densities.

In Table 4, we show the physical properties derived for the clumps. For the case of clumps *d*, *e f*, and *g* (likely associated with the inner round nebula), their volume density limits are higher than densities derived using equation 3 (see Table 3) although they are still much lower than the critical density of the CO(3−2) line (n_{crit} ∼ 10^4 cm^{-3}). This might indicate that radiative processes are also important, beside collisions, in exciting the $J = 3 \rightarrow 2$ transition of CO.

5 DISCUSSION

As mentioned in Section 2, according to the proper motions obtained by *Gaia* (Gaia Collaboration 2018), WR16 possesses a high peculiar velocity. The listed μ_α, μ_δ proper motions (Section 2) correspond to $(\mu_l, \mu_b) = (-10.52 \pm 0.06, -1.98 \pm 0.06)$ mas yr^{-1} in Galactic coordinates. Assuming that the interstellar medium local to WR16 moves in a circular orbit around the Galactic Centre, and following the procedure outlined by Comerón & Pasquali (2007) to take into account the proper motion of the local ISM, we obtain for WR16 the following peculiar proper motions (with respect to its local interstellar medium):

μ_α(pec) = −4.44 ± 0.53 mas yr^{-1},

μ_δ(pec) = 1.90 ± 0.41 mas yr^{-1},

and the corresponding spatial velocity components are

v_α(pec) = −55.2 ± 7.6 km s^{-1},

v_δ(pec) = 25.6 ± 6.5 km s^{-1}.

The peculiar tangential velocity of the star is then v_{tan} = 60.8 ± 7.4 km s^{-1} and implies that WR16 is a runaway star. As pointed out

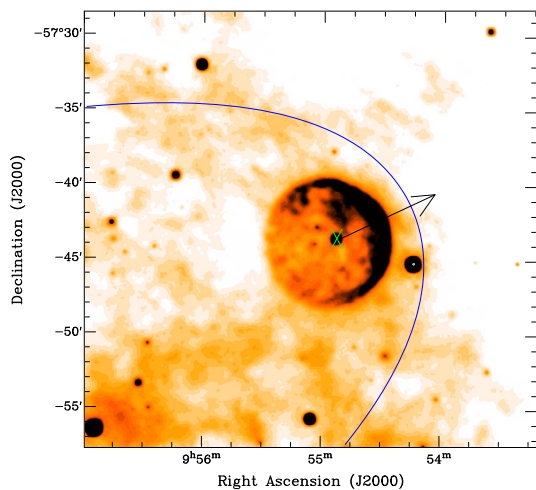**Figure 8.** Bow shock structure projected on an IR image at 22 μm. The arrow shows the direction of the tangential component of the peculiar stellar motion. The green cross indicates the location of WR16.

Figure 9. *Herschel* emission at 160 μm with superimposed NANTEN CO contours at 2, 3, and 4 K km s^{-1}, defining the Component 1 as described in [Paper I].

in Section 2, this was first suggested by Moffat et al. ([1998]) using *Hipparcos* data, from which they estimated for WR16 a peculiar tangential velocity of 123.9 $\pm$ 44.3 km s^{-1}. The discrepancy with our result is likely due to the fact that the authors used different proper motion values; also, they adopted a greater distance for WR 16. It is important to note, however, that the direction of the peculiar motion of the star does not change significantly when proper motion measurements of different accuracies are used. Given that the peculiar velocity of WR 16 is much higher than the sound speed in the neutral atomic gas ($\sim$1 km s^{-1}), the interaction of the stellar wind with the ISM is expected to give raise to a bow-shock structure, as observed around several runaway stars (e.g. Peri, Benaglia & Isequilla [2015]). To model the bow-shock structure, we follow Wilkin ([1996]) and assume a homogeneous interstellar medium with density n_0, and an isotropic stellar wind with constant mass-loss rate $\dot{M}$ and terminal velocity v_∞. The resulting structure should have a paraboloidal shape, with the stellar velocity vector as its symmetry axis. In this idealized model, the bow shock is at a distance $R(\theta)$ from the star, where $R(\theta) = R_0 \csc \theta \sqrt{(3(1 - \theta \cot \theta)}$, and θ is the polar angle measured from the symmetry axis with the star at the coordinate origin. The bow shock stand-off distance ($\theta = 0°$) sets the length-scale and is given by $R_0 = \sqrt{\dot{M} \, v_\infty / 4 \, \pi \, n_0 \, v_{\text{tan}}^2}$.

For WR16, adopting $\dot{M} = 3.2 \times 10^{-5}$ M$_\odot$ yr^{-1} (Crowther [2007]), $v_\infty = 630$ km s^{-1} (Toalá et al. [2015]), and assuming an ambient density $n_0 = 1$ cm^{-3} (roughly coincident with a uniform distribution of the mass derived in [Paper I] for Component 1 over a sphere of $\sim$15 pc in radius), we obtain $R_0 = 1.3 \pm 0.2$ pc, which at a distance of 2655 pc corresponds to $\sim$5 arcmin. Fig. 8 shows the bow-shock structure rotated according to the direction of motion of WR16, projected on to the emission distribution at 22 μm. In what follows, we analyse the infrared, radio continuum, and molecular observed structures in the context of a moving star that has gone through different evolutionary phases.

In Section 4.1, we have pointed to two striking structures in the infrared emission that may be related to the action of WR16 upon the ISM: the round nebula and the arc-shaped structure.

Based on our estimates of T_{d} (see Section 4.1), the dust in the round nebula around the WR star is probably related to the previous LBV phase, while the cold arc-like nebula is likely related to an earlier stage. In line with this scenario, the projected angular
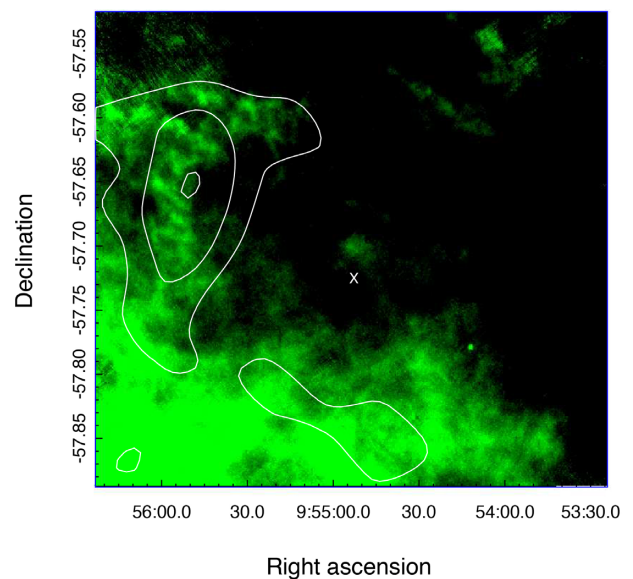
distance between the star and the apex of the bow-shock is about 5 arcmin, (see Fig. 8). This value is similar to the radius of the round nebula ($\sim$4.5 arcmin) and could explain the brighter infrared emission in the area where the nebula may have encountered the apex of a bow-shock structure, which was created before the star entered the LBV phase.

Regarding the arc-like feature, it is found to lie at the same location as the molecular structure called Component 1 in [Paper I], as shown in Fig. 9. Assuming a projected angular distance of about 9.5 arcmin (or 7.4 pc for a distance of 2655 pc) between the star and the arc-like feature, and considering a conservative expansion velocity range between 5 and 12 km s^{-1}([Paper I]), we infer a kinematical age in the range (0.6–1.5) $\times$ 10^6 yr for this structure. Thus, it is reasonable to assume that both the molecular feature and the cold dust are located at the same distance and were likely either created during the main-sequence phase of WR16, or they are the remains of the parental molecular cloud.

In Section 4.2, we highlighted a radio continuum feature strikingly lying over the bright arc in the edge of the ring nebula around WR16 (Fig. 6). The outer contour of this feature is well above the noise in the map, which together with its peculiar location and alignment with the proper motion direction of WR16, suggests that this feature is real. Bow shocks are expected to emit radio waves via the synchrotron mechanism (Benaglia et al. [2010]; del Valle & Pohl [2018]), where particles are accelerated by diffusive shock acceleration at the reverse shock. So far, the only clear observational case supporting this model is the bow shock BD $+43°3654$ (Benaglia et al. [2010]). Peri et al. ([2015]) performed a systematic search for radio features towards bow shocks detected in the infrared using the NRAO/VLA Sky Survey (NVSS) and found a few cases (3 out of $\sim$40) displaying very interesting features, a sample that was increased by four more cases after reprocessing ATCA archival data towards RCW 49. The morphology, intensity, and location of the radio feature that we observe over the ring nebula bright arc quite resembles those features reported in Peri et al. ([2015]). Hence, we propose that a bow-shock scenario is suitable

to describe the structures observed around WR16 throughout the different wavelengths analysed here.

From the molecular analysis, we identified several clumps in the region around WR16. While clumps *a*, *b*, and *c* are most probably part of a more extended molecular structure (Component 1 in Paper I), clumps *d*, *e*, *f*, and *g* appear to be associated with the round nebula on the basis of morphological considerations. The velocity of these four clumps, around ∼–9.4 km s^{-1}, strongly suggests that they represent the CO(3−2) counterpart of the CO(1−0) structure identified in Paper I as Component 3. Regarding clumps *d*, *e*, *f*, and *g*, they are located at the border where the round nebula is denser and may act as a shielding dusty envelope allowing the existence of molecular gas close to the LBV star. Based on their morphological correspondence with the optical and IR emission of the round nebula, the origin of clumps *d*, *e*, *f*, and *g* could be associated with mass eruptions of a stage previous to the WR phase, very likely a LBV stage. Indeed, their masses fall within the range of those expected in LBV outbursts (Smith & Owocki 2006; Rizzo et al. 2008). We note, however, the lack of any kinematical feature like line broadening or gradients in the molecular emission. In fact, the width of the CO lines in clumps *d*, *e*, *f*, and *g* (<2 km s^{-1}) are lower that those detected in molecular gas associated with stellar ejecta (e.g. Rizzo et al. 2008). In that regard, we can speculate that clumps *d*, *e*, *f*, and *g* could be two-dimensional projections of more spherical structures. The relatively low density of the molecular gas (see Section 4.3) could be allowing the detection of molecular emission only at the borders of the structure (limb brightening) where the radial components of the expansion velocity are negligible. A low-velocity expansion scenario could also provide an explanation for the observed line width of the clumps. More sensitive molecular observations could shed some light on this issue.

6 SUMMARY

We have analysed the infrared, radio continuum, and molecular emission in the surroundings of the runaway star WR16 using new and public data that became available recently and allowed us to improve our analysis of this region. We have discovered that this star has been affecting its local ISM along its different evolutionary phases, as could be interpreted from the observed features. In this sense, we suggest that during its main-sequence phase the star has swept-up the interstellar gas forming the molecular feature named in Paper I as Component 1, likely associated with the IR structure dubbed in this work as arc-like feature, which is composed by cold dust at ∼11 K. Three molecular clumps were identified to be associated with this feature having a total mass of at least 8 M$_\odot$. These clumps are likely tracing only the less dense molecular gas and regions of Component 1 closer to WR 16.

At the same time, due to the stellar high peculiar velocity, estimated to be $v_{tan} = 60.8 \pm 7.4$ km s^{-1}, a bow-shock structure was probably created around the star. A radio continuum analysis revealed hints supporting this hypothesis, and we explored a model which reasonably matches the emission at 22 μm. In this scenario, the star has became an LBV and experienced mass eruptions. Finally, we estimated the dust temperature and mass of the round nebula to be ∼65 K and 6.7×10^{-4} M$_\odot$, respectively, typical of LBV wind driven nebulae. Four molecular clumps were identified to be associated with the round nebula on the basis of morphological considerations. The total mass of them being at least 10 M$_\odot$, which is the range of masses expected to be released during the LBV phase. We interpret that the fast wind of the Wolf–Rayet phase has swept-up the gas ejected during the LBV stage forming the round

nebula, as revealed by the infrared emission distribution and the molecular clumps we propose to be associated with it.

REFERENCES

Agliozzo C., Noriega-Crespo A., Umana G., Flagey N., Buemi C., Ingallinera A., Trigilio C., Leto P., 2014, MNRAS, 440, 1391
Agliozzo C. et al., 2019, A&A, 626, A126
Arnal E. M., 1992, A&A, 254, 305
Bailer-Jones C. A. L., Rybizki J., Fouesneau M., Mantelet G., Andrae R., 2018, AJ, 156, 58
Benaglia P., Romero G. E., Martí J., Peri C. S., Araudo A. T., 2010, A&A, 517, L10
Bertsch D. L., Dame T. M., Fichtel C. E., Hunter S. D., Sreekumar P., Stacy J. G., Thaddeus P., 1993, ApJ, 416, 587
Bloemen J. B. G. M. et al., 1986, A&A, 154, 25
Cichowolski S., Pineault S., Arnal E. M., Cappa C. E., 2008, A&A, 478, 443
Comerón F., Pasquali A., 2007, A&A, 467, L23
Crowther P. A., 2007, ARA&A, 45, 177
del Valle M. V., Pohl M., 2018, ApJ, 864, 19
Digel S. W., Grenier I. A., Heithausen A., Hunter S. D., Thaddeus P., 1996, ApJ, 463, 609
Duronea N. U., Arnal E. M., Bronfman L., 2013, A&A, 551, A71, (Paper I)
Ezawa H. et al., 2008, in Larry M. S., Roberto G., Helen J. H., eds, Proc. SPIE Conf. Ser. Vol. 7733, Ground-based and Airborne Telescopes II. SPIE, Belligham, p. 701208
Ezawa H., Kawabe R., Kohno K., Yamamoto S., 2004, in Oschmann J. M., Jr, ed., Proc. SPIE Conf. Ser. Vol. 5489, Ground-based Telescopes. SPIE, Bellingham, p. 763
Fowler J. W., Aumann H. H., 1994, in Terebey S., Mazzarella J. M., eds, Science with High Spatial Resolution Far-Infrared Data, JPL, Pasadena, p. 1
Gaia Collaboration, 2018, A&A, 616, A11
Garcia-Segura G., Mac Low M.-M., 1995, ApJ, 455, 160
Goldreich P., Kwan J., 1974, ApJ, 189, 441
Hildebrand R. H., 1983, Q. J. R. Astron. Soc., 24, 267
Hunter S. D. et al., 1997, ApJ, 481, 205
Hutsemekers D., 1997, in Nota A., Lamers H., eds, ASP Conf. Ser. Vol. 120, Luminous Blue Variables: Massive Stars in Transition. Astron. Soc. Pac., San Francisco, p. 316
Jiménez-Esteban F. M., Rizzo J. R., Palau A., 2010, ApJ, 713, 429
Kalberla P. M. W. et al., 2010, A&A, 521, A17
Kalberla P. M. W., Haud U., 2015, A&A, 578, A78
Marston A. P., Morris P., 2009, in Onaka T., White G. J., Nakagawa T., Yamamura I., eds, ASP Conf. Ser. Vol. 418, AKARI, A Light to Illuminate the Misty Universe. Astron. Soc. Pac., San Francisco, p. 443
Marston A. P., Yocum D. R., Garcia-Segura G., Chu Y.-H., 1994, ApJS, 95, 151
Marston A. P., Welzmiller J., Bransford M. A., Black J. H., Bergman P., 1999, ApJ, 518, 769
McClure-Griffiths N. M. et al., 2009, ApJS, 181, 398
McClure-Griffiths N. M., Dickey J. M., Gaensler B. M., Green A. J., Haverkorn M., Strasser S., 2005, ApJS, 158, 178

Megier A., Strobel A., Galazutdinov G. A., Krełowski J., 2009, A&A, 507, 833

Moffat A. F. J. et al., 1998, A&A, 331, 949

Murphy T., Mauch T., Green A., Hunstead R. W., Piestrzynska B., Kels A. P., Sztajer P., 2007, MNRAS, 382, 382

Nota A., Pasquali A., Marston A. P., Lamers H. J. G. L. M., Clampin M., Schulte-Ladbeck R. E., 2002, AJ, 124, 2920

Oka T., Onodera Y., Nagai M., Tanaka K., Matsumura S., Kamegai K., 2012, ApJS, 201, 14

Parker Q. A. et al., 2005, MNRAS, 362, 689

Peri C. S., Benaglia P., Isequilla N. L., 2015, A&A, 578, A45

Rizzo J. R., Jiménez-Esteban F. M., Ortiz E., 2008, ApJ, 681, 355

Sault R. J., Teuben P. J., Wright M. C. H., 1995, in Shaw R. A., Payne H. E., Hayes J. J. E., eds, ASP Conf. Ser. Vol. 77, Astronomical Data Analysis Software and Systems IV. Astron. Soc. Pac., San Francisco, p. 433

Scoville N. Z., Solomon P. M., 1973, ApJ, 180, 31

Smith N., Owocki S. P., 2006, ApJ, 645, L45

Solomon P. M., Rivolo A. R., Barrett J., Yahil A., 1987, ApJ, 319, 730

Stock D. J., Barlow M. J., Wesson R., 2011, MNRAS, 418, 2532

Strong A. W., Mattox J. R., 1996, A&A, 308, L21

Toalá J. A., Arthur S. J., 2011, ApJ, 737, 100

Toalá J. A., Guerrero M. A., 2013, A&A, 559, A52

Toalá J. A., Guerrero M. A., Ramos-Larios G., Guzmán V., 2015, A&A, 578, A66

Toalá J. A., Marston A. P., Guerrero M. A., Chu Y.-H., Gruendl R. A., 2017, ApJ, 846, 76

van der Hucht K. A., 2001, New Astron. Rev., 45, 135

van der Sluys M. V., Lamers H. J. G. L. M., 2003, A&A, 398, 181

Weaver R., McCray R., Castor J., Shapiro P., Moore R., 1977, ApJ, 218, 377

Wilkin F. P., 1996, ApJ, 459, L31

This paper has been typeset from a TEX/LATEX file prepared by the author.